Supplemental Information

Chiral Selection of Purely Localized and Delocalized States in Non-Hermitian Photonic Waveguide Arrays

Ruiqi Wang[1], Yuliang Tang[1], Qihuang Gong[1, 2, 3, 4], and Yan Li[1, 2, 3, 4, *]

[1]*State Key Laboratory for Mesoscopic Physics and Frontiers Science Center for Nano-optoelectronics, School of Physics, Peking University, Beijing 100871, China.*

[2]*Hefei National Laboratory, Hefei 230088, China.*

[3]*Collaborative Innovation Center of Extreme Optics,*
Shanxi University, Taiyuan, Shanxi 030006, China.

[4]*Peking University Yangtze Delta Institute of Optoelectronics, Nantong 226010, China.*

* Corresponding author: li@pku.edu.cn.

Contents:

Section I: Chiral LDSS for $k = 2$ and $N > 3$

Here we consider the case $k = 2$, $N > 3$. For $N = 4, 5, 6$, the imaginary parts of the eigenenergy surfaces remain separated once the parameters evolve beyond the EPs (See Fig. S1). Consequently, throughout the entire parameter space considered, the lowest-loss energy surface remains associated with the same eigenenergy surface and does not undergo any surface exchange. Under these conditions, chiral LDSS can be achieved between two states with distinct localization characteristics via an appropriate encircling trajectory: one state is fully localized, while the other exhibits a wavefunction extending over a limited number of waveguides.

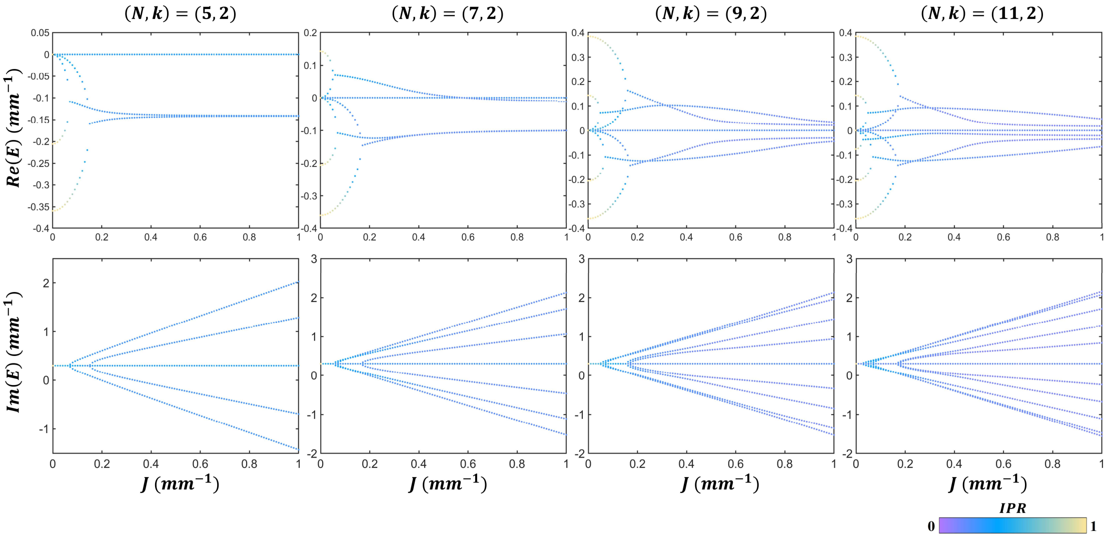

FIG. S1 Real and imaginary parts of the eigenvalue spectrum for different values of N. The other parameters are fixed at $\Delta = 0.2\ \text{mm}^{-1}$, $\phi = 0.2\pi$, $\gamma_q = \gamma_z = 0.2\ \text{mm}^{-1}$, $k = 2$.

We take $N = 5$ as an illustrative example. The real and imaginary parts of the energy surfaces are shown in Fig. S2(a), where the two EPs are marked by orange stars. The sky-blue surface corresponds to the lowest-loss energy surface, and the IPR of its eigenstates is displayed in the right panel. The encircling trajectory and the spatial distribution of ψ_1 and ψ_2 are shown in Fig. S2(b). Regardless of the input, the output mode is always ψ_1 $(IPR_1 = 1)$ for CW encircling direction (Fig. S2(c)), and ψ_2 $(IPR_2 = 0.5)$ for CCW encircling direction (Fig. S2(d)). The normalized intensity dynamics under both local and uniform excitation (Fig. S2(e)) further confirm that the encircling direction alone determines the final state.

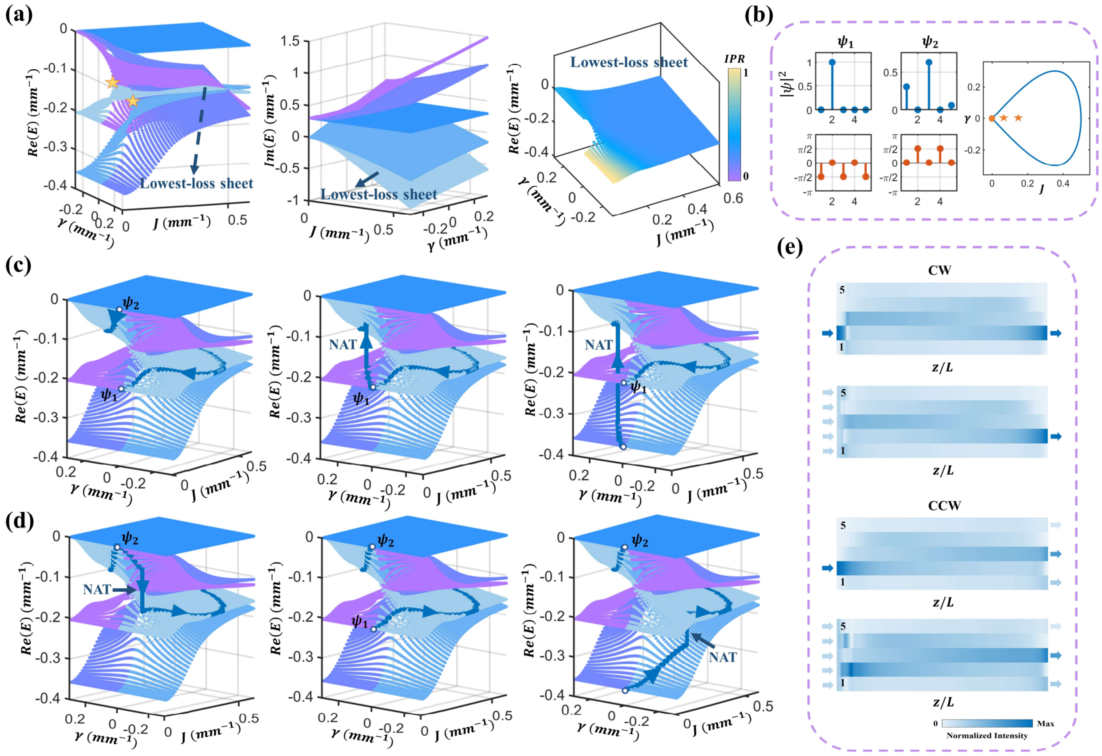

FIG. S2 Simulated results of the chiral LDSS for $k = 2$ and $N = 5$. (a) The real and imaginary parts of energy surfaces in the $J - \gamma$ parameter space. The IPR of eigenstates on the lowest-loss energy surface are calculated. (b) The encircling trajectory and the distribution of eigenstates at the starting point. (c), (d) Mode conversion results for the CW (c) and CCW (d) encircling direction with input modes ψ_1 and ψ_2. (e) The dynamics of the normalized intensity evolution at each site for CW (top) and CCW (bottom) encircling processes.

For $N \geq 7$, some imaginary parts of the eigenenergy surfaces associated with different branches become very close beyond the EPs and intersect for appropriate parameter values (see Fig. S1). As a result, the identity of the lowest-loss energy surface can switch between different eigenenergy surfaces across the parameter space. Figure S3(a) presents the real and imaginary parts of the energy surfaces for $N = 9$. One observes that the imaginary part of the secondary lowest-loss (2LS) energy surface is nearly indistinguishable from that of the lowest-loss one (1LS); in fact, the two correspond to intersecting eigenenergy surfaces. This behavior is further revealed by the real parts: the identity of the lowest-loss energy surface is associated with two distinct eigenenergy surfaces, depending on the region of parameter space. We show that this property leads to enhanced selectivity for chiral LDSS.

When the encircling trajectory approaches the critical parameter regime (gray-blue area) where the identity of the lowest-loss surface switches (e.g., the encircling trajectory shown in Fig. S3(b)), the chiral conversion occurs between distinct pairs of eigenstates: ψ_1 ($IPR_1 = 1$) and ψ_2 ($IPR_2 = 0.521$), as well as ψ_3 ($IPR_3 = 1$) and ψ_4 ($IPR_4 = 0.530$). This behavior is enabled by the near-degeneracy in loss (imaginary part) of the eigenenergy surfaces occupied by these two pairs of states within this parameter range. Crucially, the initial excitation site determines which pair participates in the dynamics. For example, when site 1 is excited, the output mode is ψ_1 for CW encircling and ψ_2 for CCW encircling. When site 8 is excited, the output mode is ψ_3 for CW encircling and ψ_4 for CCW encircling. Thus, the output state is jointly controlled by the encircling direction and the excitation profile.

When the encircling trajectory remains well within the parameter regime preceding the switching area (as shown in Fig. 3(c)), the output mode for CW is always ψ_3. For CCW encircling, the output is predominantly ψ_4, although ψ_2 may appear with a small probability depending on the initial excitation. This behavior arises because the eigenenergy branch hosting ψ_3 and ψ_4 constitutes the unambiguously dominant lowest-loss surface in this regime, and NATs subsequently drive the system to evolve stably on it.

When the encircling trajectory extends well beyond the critical switching position (see Fig. 3(d)), chiral conversion becomes confined to the pair ψ_1 and ψ_2. This restriction arises because their eigenenergy surface emerges as the dominant lowest-loss branch over most of the parameter range. NATs drive the system onto this branch, where it subsequently evolves stably. Consequently, the output is universally determined by the encircling direction: ψ_1 for CW encircling direction and ψ_2 for CCW encircling direction.

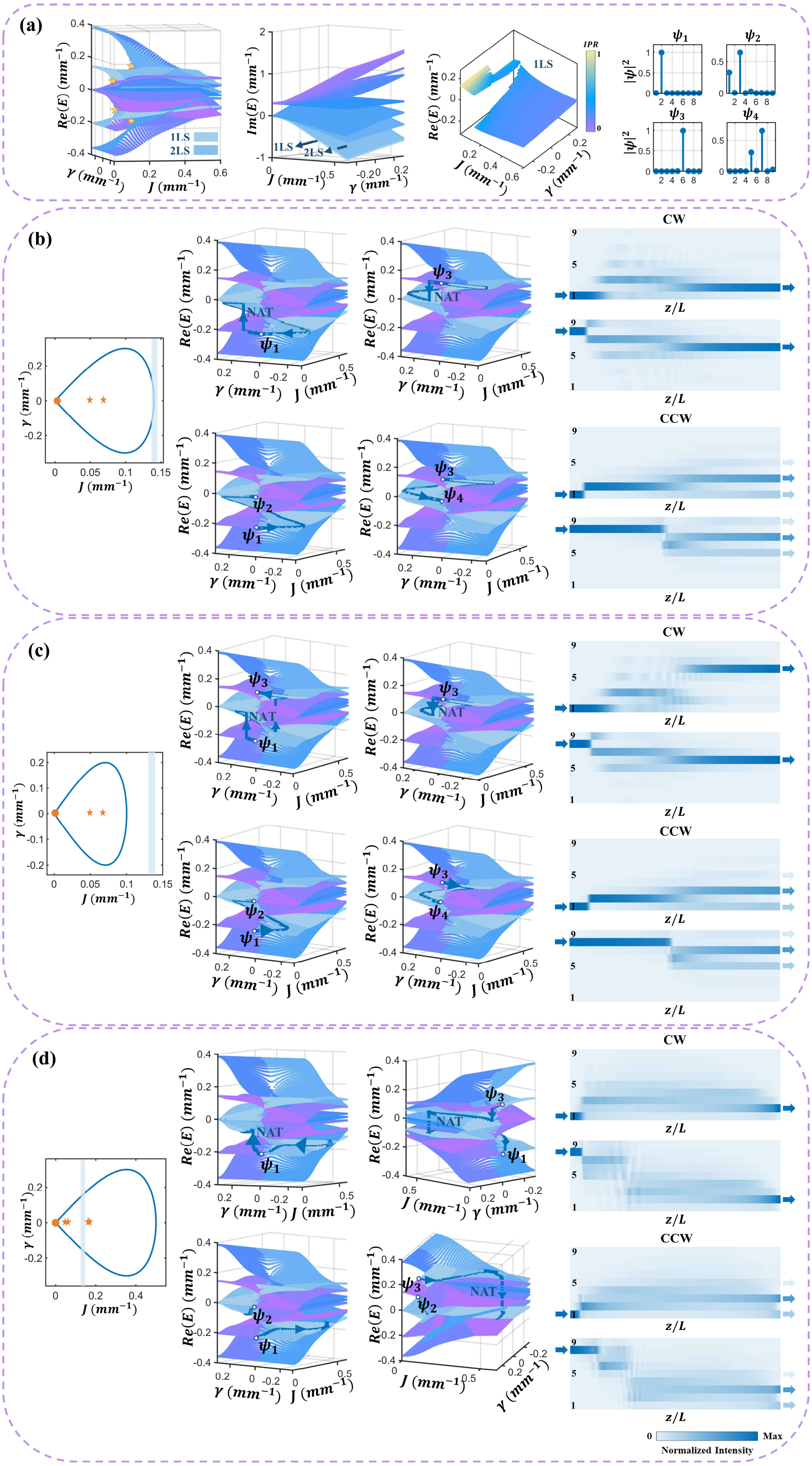
(a)
$Re(E)$ (mm^{-1})
γ (mm^{-1})
J (mm^{-1})
1LS
2LS
$Im(E)$ (mm^{-1})
IPR
ψ_1
ψ_2
ψ_3
ψ_4
$|\psi|^2$
(b)
NAT
CW
CCW
z/L
(c)
(d)
0
Max
Normalized Intensity

FIG. S3 Simulated results of the chiral LDSS for $k = 2$ and $N = 9$. (a) The real and imaginary parts of energy surfaces in the $J - \gamma$ parameter space. The IPR of eigenstates on the lowest-loss energy surface are calculated. The rightmost inset shows the distribution of eigenstates involved in the chiral mode conversion. (b), (c), (d) Mode conversion for three encircling conditions relative to the critical regime (gray-blue area). (b) Approaching, (c) before, and (d) beyond the critical regime. Left panels: schematic of the encircling trajectories. Middle panels: state evolution for input state ψ_1 and ψ_3. Right panels: the dynamics of the normalized intensity evolution at each site when site 1 or site 8 is excited.

Section II: Chiral LDSS for different (N, k)

For $(N, k) = (13,7)$, we present the state evolution under different initial excitation conditions. Figure S4 shows the normalized intensity dynamics for both CW and CCW encircling processes.

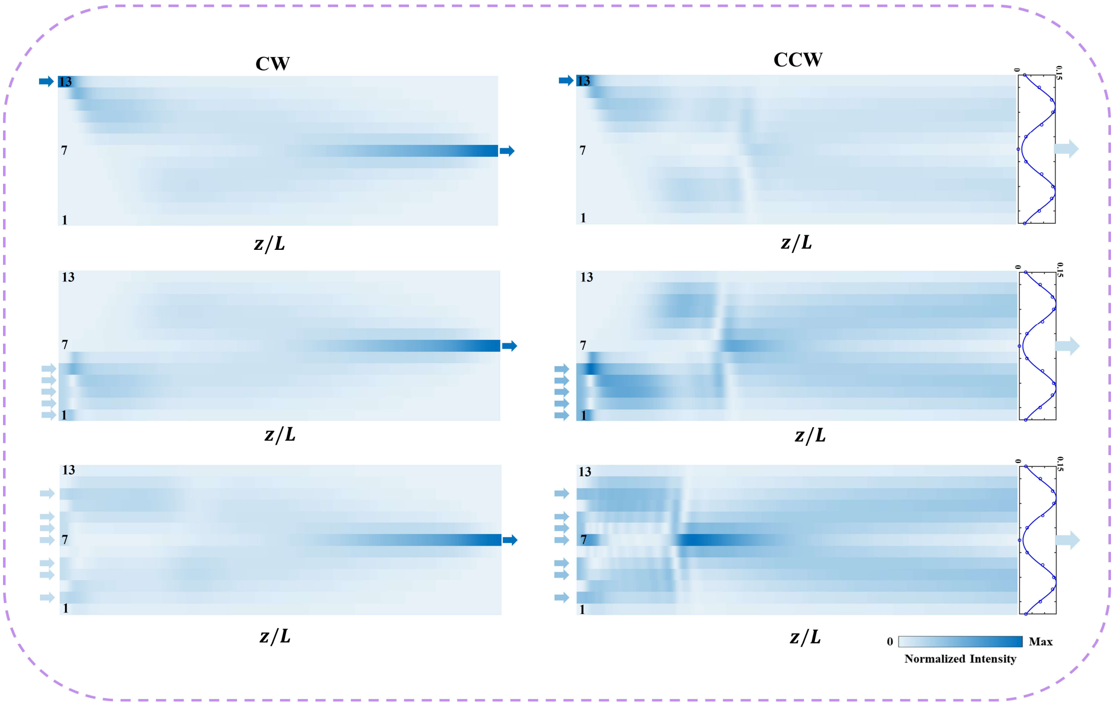

FIG. S4 Dynamics of the normalized intensity evolution for CW (left) and CCW (right) encircling processes upon different initial excitations.

To demonstrate the universality of the chiral LDSS between the localized state ψ_L and the delocalized state ψ_D, whose wavefunction follows a double-Gaussian distribution, we further examine additional parameter combinations (N, k) satisfying $k = (N + 1)/2$. The corresponding results are presented in Fig. S5.

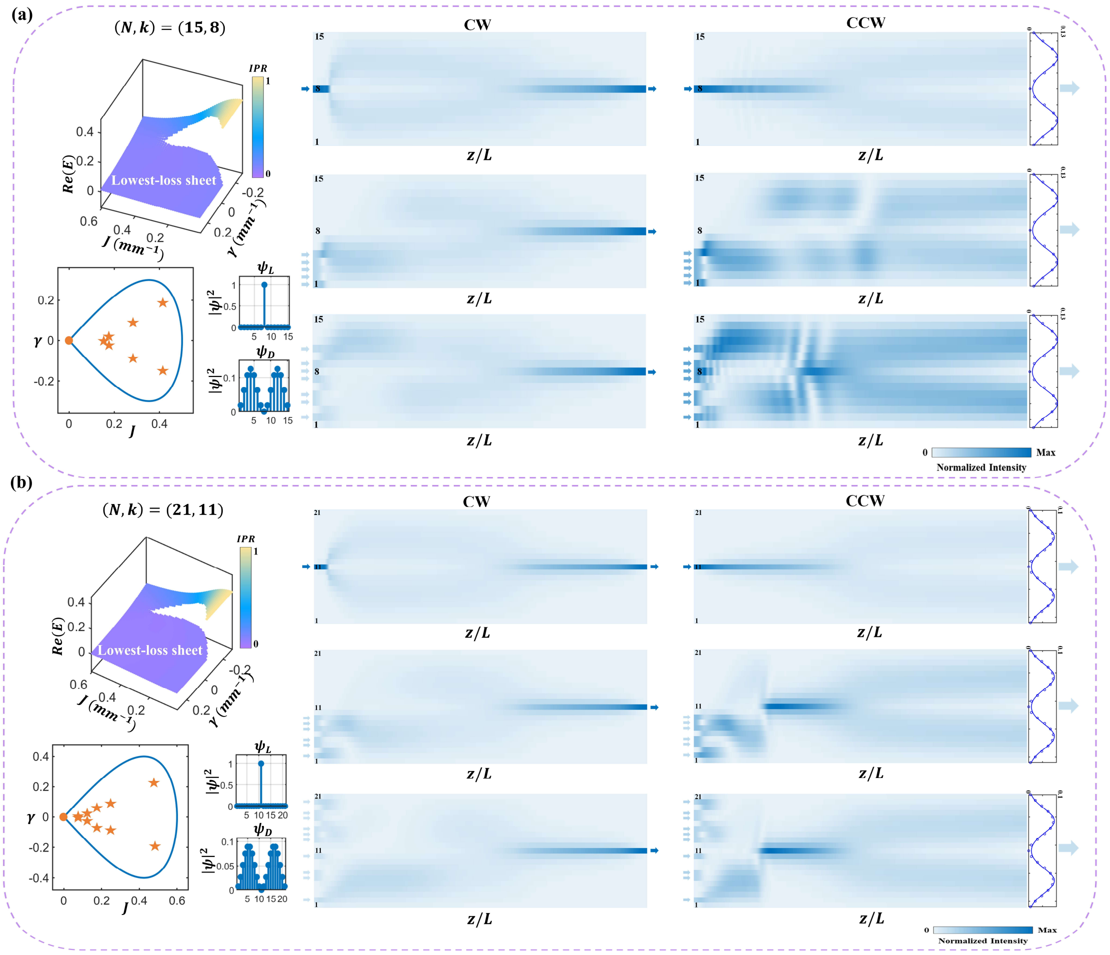

FIG. S5 Simulated results of the chiral LDSS for (a) $(N,k)=(15,8)$ and (b) $(N,k)=(21,11)$. Left panels: calculated IPR of the eigenstates on the lowest-loss energy surface, the encircling trajectory, and the spatial distributions of ψ_L and ψ_D. Right panels: CW/CCW encircling dynamics (normalized intensity) for different initial excitations.

Section III: The translation from the theoretical model to the experimental system

(1) Equivalent process from H_2 to H_1

Here, we provide the rationale for using H_2 as an effective equivalent of H_1 in the main text. We impose the conditions $\beta_1=\beta_5$ and $\beta_2=\beta_4$, such that H_2 becomes centrosymmetry. Under these conditions, H_2 can be partitioned into two 3×3 blocks, as illustrated in Fig. S6(a). Under the adiabatic elimination condition $\gamma \gg |\kappa_{1,2}|$, each block can be reduced to an effective 2×2 Hamiltonian, which has been analyzed in detail within the coupled-mode theory framework[1]. If the additional conditions $\gamma \gg |\beta_2-\beta_1|$ and $\gamma \gg |\beta_2-\beta_3|$ are satisfied, the Hamiltonian H_{eff} can be obtained (Fig. S6(a)). By defining the effective parameters $\beta = \beta_3 - \beta_1$, $J = \frac{\kappa_1\kappa_2}{\gamma}$, $\gamma_z = \frac{\kappa_1^2}{\gamma}$ and $\gamma_q = \frac{\kappa_2^2}{\gamma}$, we finally recover the Hamiltonian H_1. Figure S6(b) illustrates the simulated mode conversion processes based on H_2. For the CW encircling processes, the dynamic evolution consistently directs light to a single output port WG3, regardless of the input excitation. For the CCW encircling processes, light is output exclusively and equally from WG1 and WG5. The chiral transmission efficiency, defined as the maximum transmittance across all conversion processes, is 24.7% (Fig. S6(c)).

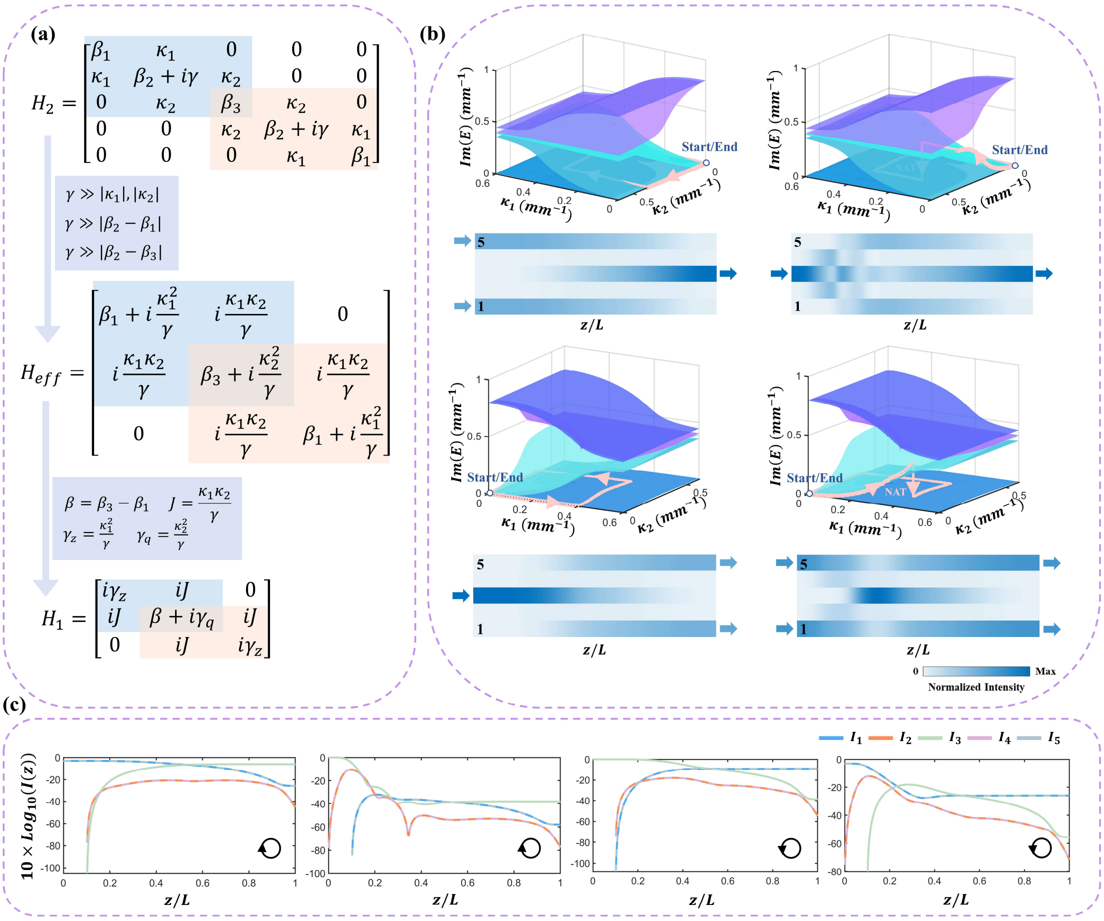

FIG. S6 (a) Equivalent process from H_2 to H_1. (b) The simulated mode conversion processes for CW (top) and CCW (bottom) encircling directions based on H_2. The encircling trajectory is identical to that shown in Fig. 4(b) of the main text. The other parameters are set as $\beta_1 = 0$, $\beta_2 = 0.103\ \mathrm{mm}^{-1}$, $\beta_3 = 0.206\ \mathrm{mm}^{-1}$, $\gamma = 0.8\ \mathrm{mm}^{-1}$, $L = 50$ mm. Here, the values of $\beta = \beta_3 - \beta_1$ are chosen according to the quasiperiodic modulation formula $\beta = 2\Delta\cos(4\pi b + \phi)$, while γ is selected to satisfy the adiabatic elimination condition $\gamma \gg |\kappa_{1,2}|$. (c) Calculation results of the intensity distribution during evolution for CW and CCW encircling directions. The total input intensity is normalized to unity, and for the simultaneous excitation of WG1 and WG5, each waveguide carries half of the total input intensity.

(2) Achieving high transmission efficiency based on H_3

Figure S7(a) presents the simulation results of chiral mode conversion based on H_3. The relative distribution of the output light intensity agrees well with that obtained from H_2, while the transmission efficiency is markedly improved, reaching 78.1% compared with the low-efficiency case discussed above (Fig. S7(b)). This enhancement arises because the path-dependent loss is largely suppressed, since the imaginary part of the system's lowest-loss energy surface is equal to zero. This efficiency can be further improved toward unity by increasing either the total evolution length L or the maximum coupling coefficient κ_{max} along the trajectory, as shown in Fig. S7(c) ($L = 50$ mm, $\kappa_{max} = 0.4\ \mathrm{mm}^{-1}$ in the main text).

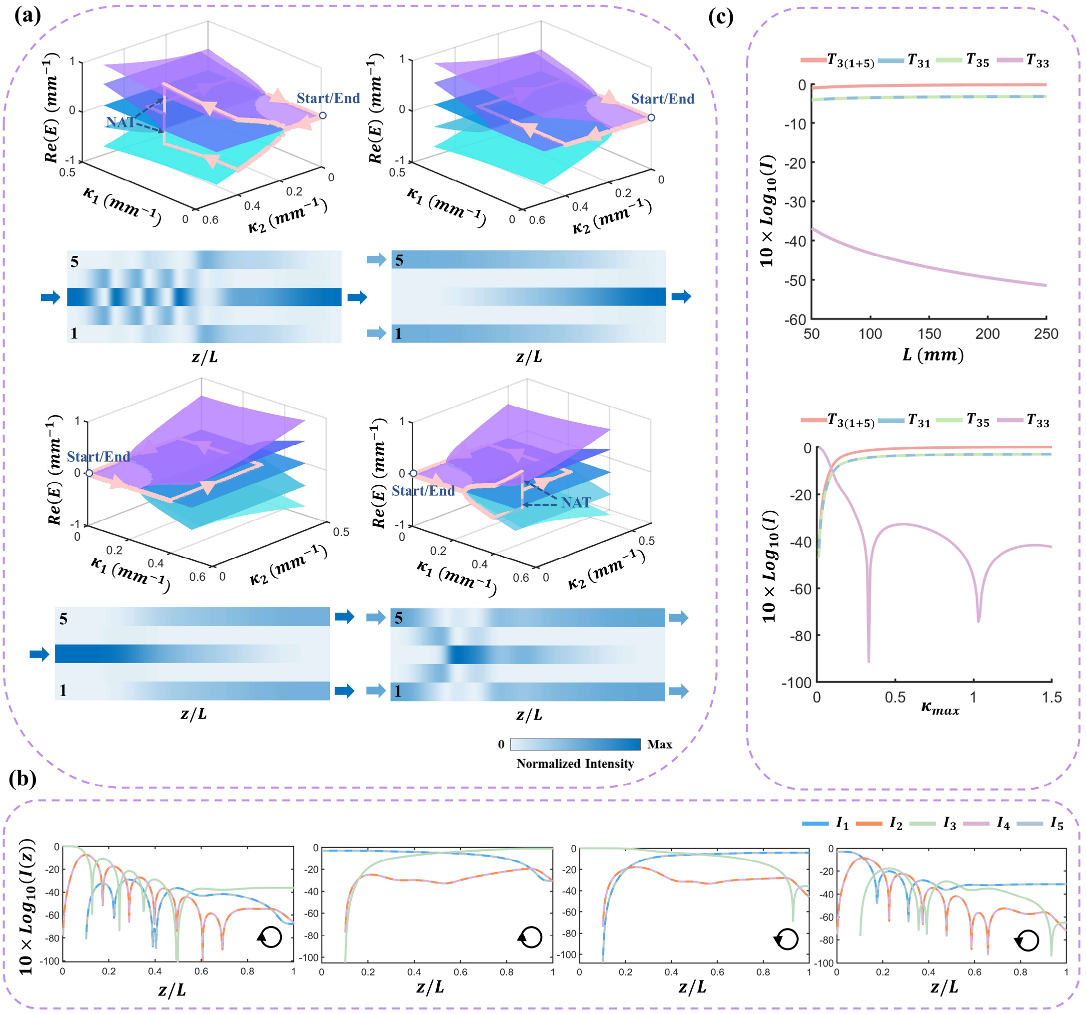

FIG. S7 (a) Mode conversion for CW (top) and CCW (bottom) encircling directions, simulated using the EL encircling approach ($L = 50$ mm). (b) Calculation results of the intensity distribution during evolution for CW and CCW encircling directions. The total input intensity is normalized to unity, and for the simultaneous excitation of WG1 and WG5, each waveguide carries half of the total input intensity. (c) Transmittance T for CW encircling versus propagation distance L (top, $50-250$ mm) and the maximum coupling coefficient κ_{max} (bottom, $0-1.5\ \mathrm{mm}^{-1}$). Here, T_{mn} denotes the transmittance from input WGn to output WGm. Specifically, WG(1+5) labels the condition of equal intensity distribution in WG1 and WG5. The chiral transmission efficiency $T_{3(1+5)}$ (maximum transmittance) increases with both z and κ_{max}.

Section IV: Optical field evolution in a practical EL encircling waveguide structure

In our experiment, we use the FLDW to fabricate 3D optical waveguide structures inside glass to realize the dynamic encircling process. The entire EL encircling waveguide structure is embedded inside glass, making it challenging to monitor the light intensity evolution in individual waveguides directly and in real time. In this section, we utilize the Beam Propagation Method (BPM) to demonstrate the evolution of the mode fields within the five-waveguide EL encircling structure (Fig. S8), with parameters set to ensure single-mode propagation at 785 nm. The simulation encompasses the entire five-waveguide structure, including the auxiliary region and the EL encircling region. For the CW encircling direction, the five-waveguide system consistently outputs through WG3 regardless of input state, functioning as an optical combiner. In the CCW process, the system distributes the output almost equally between WG1 and WG5, regardless of the input port, thereby functioning as a beam splitter. For cases with intense oscillations during evolution (such as when WG3 is excited under CW encircling), a significant portion of energy is dissipated through the lossy waveguides (WG2 and WG4), leading to very low output intensity. By normalizing the intensity distribution within each waveguide at every position, we can more clearly observe the oscillation process, as illustrated in the inset.

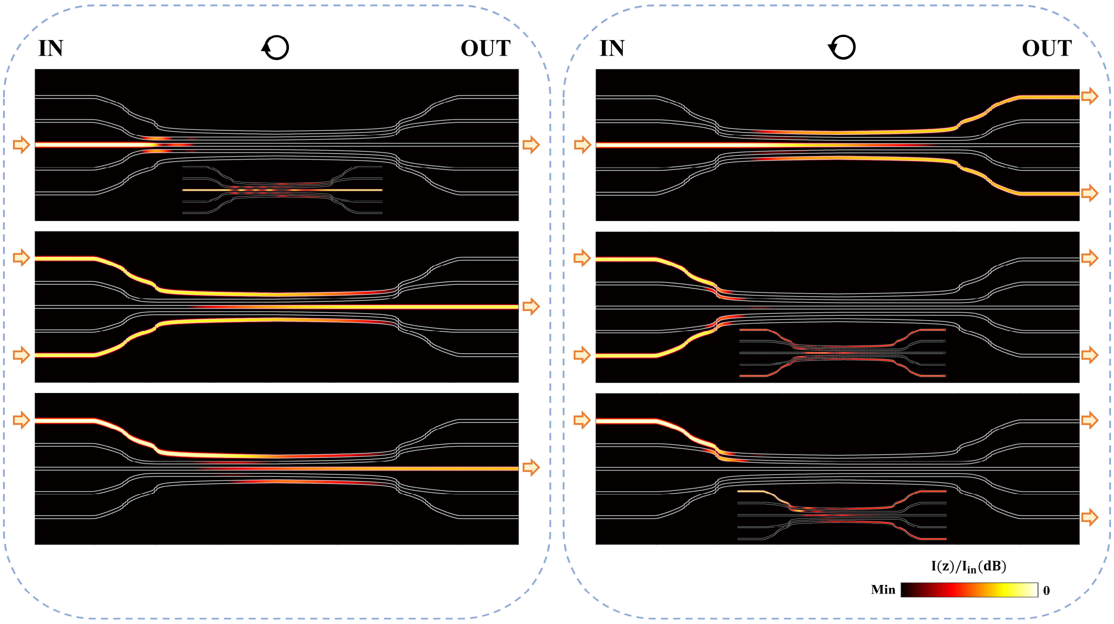

FIG. S8 Optical field evolution within the five-waveguide EL encircling structure of chiral LDSS for CW and CCW encircling processes via the Beam Propagation Method.

Section V: Realization of the $(N, k) = (5, 3)$ case using a nine-waveguide system

Here, we demonstrate the equivalence of the $(N, k) = (5, 3)$ case using a nine-waveguide system. The Hamiltonian of the nine-waveguide system is:

$$H_{9WG} = \begin{bmatrix} 0 & \kappa_1 & 0 & 0 & 0 & 0 & 0 & 0 & 0 \\ \kappa_1 & i\gamma & \kappa_1 & 0 & 0 & 0 & 0 & 0 & 0 \\ 0 & \kappa_1 & 0 & \kappa_1 & 0 & 0 & 0 & 0 & 0 \\ 0 & 0 & \kappa_1 & i\gamma & \kappa_2 & 0 & 0 & 0 & 0 \\ 0 & 0 & 0 & \kappa_2 & \beta & \kappa_2 & 0 & 0 & 0 \\ 0 & 0 & 0 & 0 & \kappa_2 & i\gamma & \kappa_1 & 0 & 0 \\ 0 & 0 & 0 & 0 & 0 & \kappa_1 & 0 & \kappa_1 & 0 \\ 0 & 0 & 0 & 0 & 0 & 0 & \kappa_1 & i\gamma & \kappa_1 \\ 0 & 0 & 0 & 0 & 0 & 0 & 0 & \kappa_1 & 0 \end{bmatrix}.$$

Following the adiabatic elimination method outlined in Sec. III, we obtain the effective Hamiltonian:

$$H_e = \begin{bmatrix} i\gamma_z & i\gamma_z & 0 & 0 & 0 \\ i\gamma_z & i\gamma_z & iJ & 0 & 0 \\ 0 & iJ & \beta + i\gamma_q & iJ & 0 \\ 0 & 0 & iJ & i\gamma_z & i\gamma_z \\ 0 & 0 & 0 & i\gamma_z & i\gamma_z \end{bmatrix}.$$

Although H_e is not identical to the Hamiltonian of the target $(N, k) = (5, 3)$ system, we demonstrate that the same chiral LDSS can be achieved by choosing an appropriate encircling trajectory in the $J - \gamma_q$ parameter space. The corresponding simulation results are presented in Fig. S9.

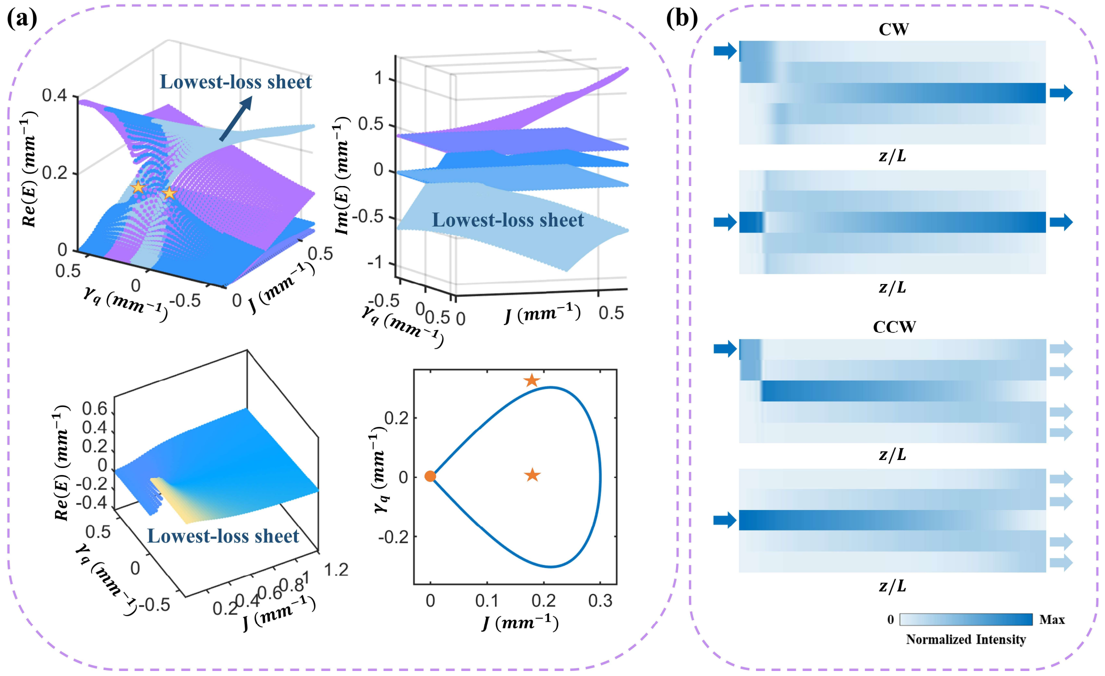

FIG. S9 Simulation results based on H_e. (a) Top: Real and imaginary parts of the energy surfaces in the $J-\gamma_q$ parameter space. Bottom: Calculated IPR of the eigenstates on the lowest-loss energy surface and the chosen encircling trajectory. The starting point (orange circle) is at $\gamma_q = 0$, $J = 0.0001\ \mathrm{mm}^{-1}$. Fully localized states on this surface exist only for $\gamma_q \le 0$. The trajectory encircles the EP on the lowest-loss surface. (b) CW/CCW encircling dynamics (normalized intensity) for different initial excitations.

In a practical waveguide structure, we set the detuning between all sites to zero. The Hamiltonian of the resulting nine-waveguide system is:

$$H_{9W}\ (z) = \begin{bmatrix} 0 & \kappa_1(z) & 0 & 0 & 0 & 0 & 0 & 0 & 0 \\ \kappa_1(z) & i\gamma & \kappa_1(z) & 0 & 0 & 0 & 0 & 0 & 0 \\ 0 & \kappa_1(z) & 0 & \kappa_1(z) & 0 & 0 & 0 & 0 & 0 \\ 0 & 0 & \kappa_1(z) & i\gamma & \kappa_2(z) & 0 & 0 & 0 & 0 \\ 0 & 0 & 0 & \kappa_2(z) & 0 & \kappa_2(z) & 0 & 0 & 0 \\ 0 & 0 & 0 & 0 & \kappa_2(z) & i\gamma & \kappa_1(z) & 0 & 0 \\ 0 & 0 & 0 & 0 & 0 & \kappa_1(z) & 0 & \kappa_1(z) & 0 \\ 0 & 0 & 0 & 0 & 0 & 0 & \kappa_1(z) & i\gamma & \kappa_1(z) \\ 0 & 0 & 0 & 0 & 0 & 0 & 0 & \kappa_1(z) & 0 \end{bmatrix}.$$

The evolution of the mode fields in this nine-waveguide EL encircling structure is simulated using the BPM (see Fig. S10). The corresponding encircling trajectory in the EL encircling region is shown in the inset. The maximum coupling coefficient $\kappa_{max} = 0.8\ \mathrm{mm}^{-1}$, and the total device length is $L = 120\ \mathrm{mm}$.

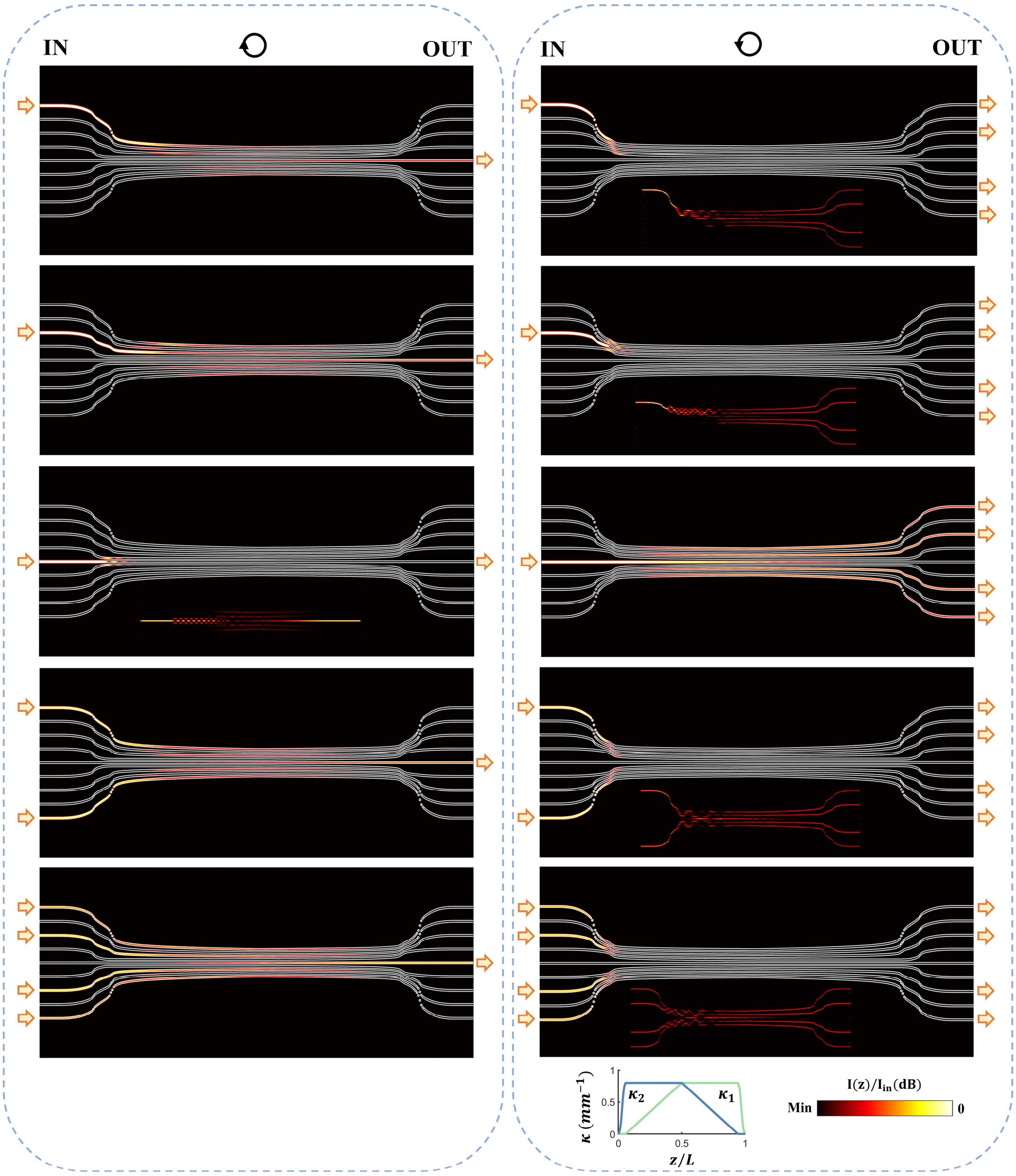

FIG. S10 Optical field evolution within the nine-waveguide EL encircling structure of chiral LDSS for CW and CCW encircling processes via the Beam Propagation Method.

Section VI: Discussion of the efficiency discrepancy between simulation and experiment

The experimentally measured transmission efficiency is generally lower than that predicted in simulation, mainly due to fabrication-related imperfections in the implementation of loss. In our experiment, the loss is introduced by writing scatterers along the propagation direction, which is relatively time-consuming during fabrication. As a result, unavoidable slight positional drifts accumulate over the writing process, leading to deviations in the actual loss from the designed value and consequently reducing the overall transmission efficiency. In addition, because the loss is realized through discrete scatterers with a spacing of 100 μm, the propagating light does not experience an ideally uniform loss throughout the dynamical evolution. This discrete implementation may further contribute to the discrepancy between experimental and simulated transmission efficiencies. These nonideal factors mainly affect the absolute transmission efficiency, but do not modify the physical mechanism demonstrated here or compromise the validity of our main conclusions. We expect that, with more precise control over the fabricated loss profile, the transmission efficiency can be further improved.

Section VII: Robustness against the deviation of $\boldsymbol{\kappa}$ and $\boldsymbol{\gamma}$

Here, we display the state conversion outcomes of 50 evolution processes in the five-waveguide EL encircling system for different excitation conditions to confirm the robustness of the system against perturbations in κ and γ. Random perturbations within $\pm 0.2\ \mathrm{mm}^{-1}$ for κ (κ_1, κ_2) and γ are added at each evolution step of every conversion process. For the CW encircling processes (see Fig. S11(a)), the system consistently outputs through WG3 regardless of input state. For the CCW encircling processes (see Fig. S11(b)), the output is distributed almost equally between WG1 and WG5, also independent of the input. Although output intensity fluctuations increase in processes involving NATs, mode crosstalk remains negligible.

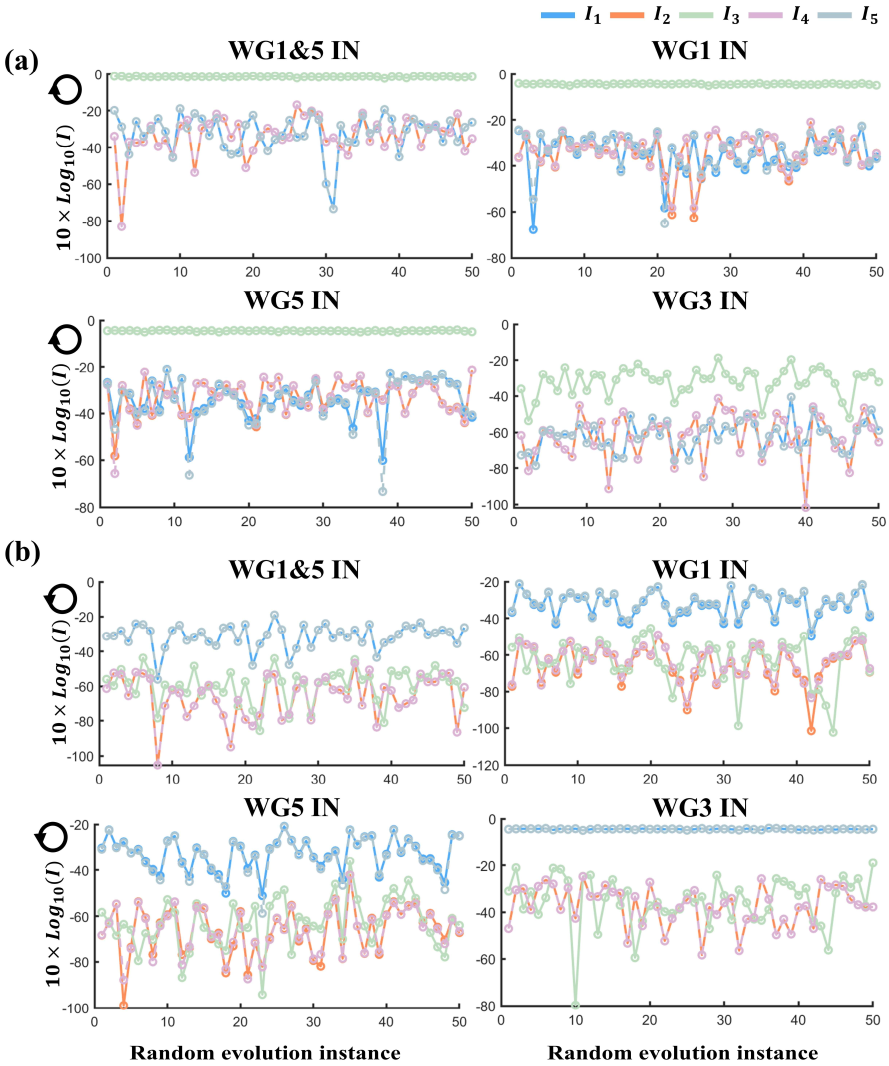

FIG. S11 Robustness of chiral LDSS in the five-waveguide EL encircling system. (a), (b) State conversion outcomes from 50 evolution processes with different excitation conditions for (a) CW and (b) CCW encircling directions. Random perturbations within $\pm 0.2\ \mathrm{mm}^{-1}$ were applied to κ_1, κ_2 and γ at each evolution step.

Reference:

1 Yang, F., Liu, Y. C. & You, L. Anti-PT symmetry in dissipatively coupled optical systems. *Phys. Rev. A* **96**, 053845 (2017).